Three-dimensional imaging of vasculature and forming quail femur using cryo-correlative light and electron microscopy (cryo-CLEM)

Anne Seewald, [ID] Jingxiao Zhong, [ID] Macarena Siri, [ID] Peter Fratzl [ID] and Emeline Raguin [ID] *

Bone mineralization during embryonic development requires the transport and deposition of an enormous amount of mineral precursors. In avian embryos, blood vessels play a dual role in this context: facilitating the demineralization of the eggshell to supply calcium and other minerals on the one hand, and mediating their deposition into the developing skeleton on the other. Understanding the interface between blood vessels and the surrounding tissues is therefore crucial for unraveling the mechanisms underlying biomineralization. However, visualizing this interface poses significant challenges and requires imaging methods that preserve the ultrastructure in a close-to-native state. Here we present a detailed methodology for a cryogenic correlative light and electron microscopy (cryo-CLEM) workflow to investigate the transport of mineral precursors in blood vessels of the femur of quail embryos during bone development. To achieve this, we use a fluorophore-conjugated antibody to label endothelial cells, which form the inner lining of blood vessels and which mediate exchanges between the bloodstream and developing tissues. This approach enables precise localization of blood vessels through fluorescence microscopy, which is subsequently correlated with 3D high-resolution electron microscopy using Focused Ion Beam-Scanning Electron Microscopy (FIB-SEM). This methodology allows imaging of a sufficient volume to observe both the lumen of the blood vessels and the surrounding matrix, providing deeper insights into calcium transport and bone mineralization during quail embryogenesis.

1. Introduction

The development of the skeletal system during embryogenesis depends on bone mineralization, which involves transporting and depositing significant quantities of calcium. This process is intricately linked to angiogenesis, the formation of blood vessels, with the vascular system providing structural support and

Department of Biomaterials, Max Planck Institute of Colloids and Interfaces, Am Mühlenberg 1, Potsdam 14476, Germany. E-mail: emeline.raguin@mpikg.mpg.de

functional regulation essential for initiating osteogenesis.[1-3] Blood vessels not only supply the necessary nutrients and oxygen to growing bones but also play a pivotal role in the transport of calcium and other mineral precursors required for skeletal formation and growth.[4,5] Endothelial cells lining these vessels facilitate these exchanges, acting as key regulators of calcium delivery to mineralization sites.[2,6,7] Despite advances in understanding the underlying molecular interactions,[8,9] the precise mechanisms by which vasculature and endothelial cells coordinate calcium transport and deposition remain poorly understood. A significant challenge lies in the visualization of these interactions in the native tissue. Traditional techniques often fail to accurately preserve ultrastructural details and/or precursor phases, thereby introducing imaging artifacts. Moreover, precisely targeting regions of interest in high-resolution microscopy presents additional challenges, which further complicates the study of these interactions. These limitations in current imaging techniques hinder our ability to comprehensively understand the intricate interplay between vascularization and mineralization, highlighting the need for the development of more advanced imaging workflows.

Cryogenic correlative light and electron microscopy (cryo-CLEM) provides a unique solution to these challenges, combining fluorescence microscopy for structural localization with electron microscopy for ultrastructural imaging under cryogenic conditions. Over the past decade, cryo-CLEM has been widely used in cell biology, primarily by preparing samples on EM grids with plunge freezing.[10,11] These grids facilitate precise correlation between fluorescence and electron microscopy by providing clear spatial references visible by both methods.[12-15] However, such grids are unsuitable for bulky or thick samples, such as bone sections, and for larger-volume imaging using cryogenic focused ion beam-scanning electron microscopy (cryo-FIB-SEM). For these bulkier samples, high-pressure freezing (HPF) is an alternative vitrification method, enabling the investigation of complex tissues in a near-native state.[16,17] Despite its potential for imaging relatively large volumes, the combination of cryo-CLEM and cryo-FIB-SEM has been applied in only a limited number of studies to date.[18,19] This may be due to the challenges of achieving accurate correlation between the two imaging modalities under cryogenic conditions, as *in situ* features are often difficult to identify from the HPF carriers. However, recent advancements have demonstrated that the use of patterned discs can effectively address this issue.[19,20]

To investigate vascularization in a non-genetically modified animal model, *in vivo* labelling of blood vessels for fluorescence microscopy is necessary to preserve its physiological state prior to HPF. However, this step is technically challenging, as it requires the delivery of fluorescent markers to the vasculature without disrupting the surrounding tissues or interfering with ongoing developmental processes.

Avian embryos, such as quail, offer a unique perspective for studying the role of blood vessels in bone mineralization due to their accessibility and close association with the eggshell *via* the chorioallantoic membrane (CAM). The CAM, a highly vascularized extraembryonic structure, is located directly beneath the eggshell and plays a critical role in mobilizing calcium for the developing embryo. Calcium from the eggshell is absorbed by the CAM vasculature and transported into the systemic circulatory system, where it is directed to mineralizing tissues.[21-25] As the embryo grows, the CAM expands and the vascular network

becomes increasingly complex, facilitating increased calcium mobilization from the eggshell into the embryonic circulation.[26]

We aim to visualize the structural organization of vascular interfaces during bone mineralization in the femur of quail embryos. Here, we present a workflow to label endothelial cells *in ovo* using fluorophore-conjugated antibodies, localize blood vessels with fluorescence light microscopy, and correlate these findings with high-resolution 3D FIB-SEM imaging under cryogenic conditions. Our standardized method for post-acquisition correlation of volumes from the two imaging modalities enables us to investigate how mineral precursors are transported within the vasculature and delivered to bone mineralization sites. This workflow also serves as a proof of concept for its application to HPF carriers.

Our findings reveal the presence of numerous vesicles containing mineral precursors within endothelial cells and blood vessels, providing new insights into the mechanisms of calcium transport and deposition. This study not only provides insights for the relationship between vasculature and bone but also establishes a robust methodological framework for further investigations into the coupling of vascular systems and skeletal development.

2. Experimental

2.1. Eggs procurement and incubation

In compliance with the German Animal Welfare Act and the Laboratory Animal Welfare Ordinance, ethics committee approval for animal experimentation was not necessary. Fertilized Japanese quail eggs (*Coturnix japonica*) were obtained from a commercial supplier (Vogelsberger Wachtelzucht GmbH, Mücke, Germany). Upon arrival, the eggshells were carefully cleaned with a 70% ethanol wipe to avoid microbial infection. The eggs were then placed in an automatic digital incubator (BRUJA Flächenbrüter 3333D, Brutmaschinen-Janeschitz GmbH, Hammelburg, GE) set to 38.5 ± 0.5 °C with $65 \pm 5\%$ relative humidity and rotated hourly. One hour following the intravascular injection of QH1 Alexa 488-conjugated antibody *in ovo*, the embryos were sacrificed by cervical dislocation and femurs were surgically removed at embryonic developmental day (EDD) 12 post-fertilization.

2.2. Fluorescence labelling technique

To target the vasculature, an unpurified monoclonal QH1 antibody was obtained from the Developmental Studies Hybridoma Bank (DSHB), Iowa. This antibody recognizes endothelial and hematopoietic stem cells.[27] Antibody purification was carried out using a Protein G HP SpinTrap™/Ab SpinTrap™ column according to the manufacturer's protocol, then concentrated by centrifugation at $10\,000g$ for 15 minutes at 4 °C using an Amicon Ultra-0.5 mL centrifuge filter unit (3 kDa cutoff). The purified antibody was then conjugated to Alexa Fluor® 488 using the Microscale Protein Labeling Kit (A30006) as per the manufacturer's instructions. The labeled antibody's concentration was measured using a NanoDrop UV-visible spectrophotometer (DS-11 FX μVolume Spectrophotometer/Fluorometer) and adjusted to 4 mg mL^{-1} for injection.

For *in ovo* intravascular injection, 500 μL of the conjugated QH1 antibody was diluted to 4 μg mL^{-1} in 1× PBS and loaded into a 1 mL syringe. The needle (TSK

1. Eggshell opening   **2. Membrane clearing**   **3. Intravascular injection**   **4. Bleeding control**

Day 0
Incubation

Day 12
In ovo intravascular
injection + harvest

Day 16/17
Hatching

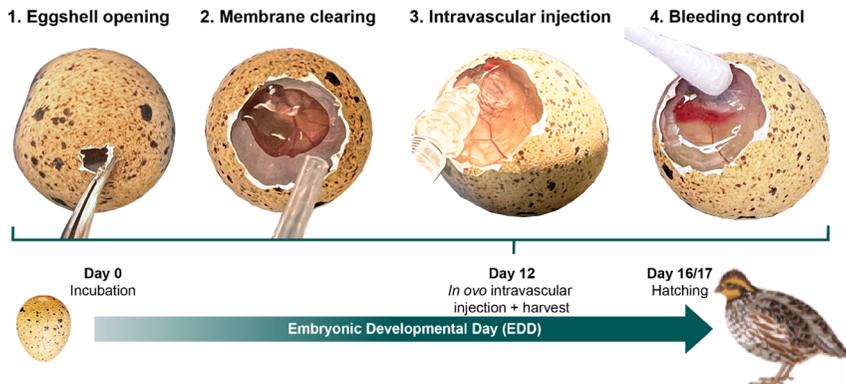**Embryonic Developmental Day (EDD)**

Fig. 1 Intravascular injection of antibodies *in ovo* at EDD12 showing the most important steps.

'The Invisible Needle', Zero Residual™) was bent to create a curved tip for easier vessel puncture. To avoid air bubbles, the syringe and needle were thoroughly vented before use. A small window was carefully created in the eggshell above the air sac by removing fragments of the shell (Fig. 1, step 1). A drop of double-distilled water was applied to the membrane to improve CAM visibility (Fig. 1, step 2) and the excess was removed with a cotton swab. A suitable vessel on the CAM, preferably a vein due to its brighter appearance and blood flow pattern, was selected. The egg was tilted to optimize the injection angle, and the needle was inserted parallel to the vessel (Fig. 1, step 3). Precision was enhanced by moistening the needle tip with a small expelled drop before insertion. Successful insertion was confirmed by the disappearance of refracted light at the injection site. After injection, the needle was carefully withdrawn, and any bleeding was controlled by applying pressure with a cotton swab soaked with a spray dressing (URGO Filmogel™) to seal the site (Fig. 1, step 4). The window was then closed with parafilm™, and the egg was returned to the incubator to maintain the embryo's viability until sacrifice 1 h after injection.

2.3. Sample preparation

Preparing cross-sections of bone just a few hundred micrometers thick can be challenging. To address this, we designed a custom double-blade guillotine capable of accurately cutting 400 μm sections at the midshaft of the quail femur at EDD12 (Fig. 2A). Each section was then immediately placed in a bottom carrier, which had been pre-marked at three distinct locations on the rim using a scalpel blade to facilitate the correlation between imaging modalities (Fig. 2B). Two configurations were used to sandwich the samples to determine whether the correlation between imaging modalities would differ as well as between aluminum *versus* gold-coated carriers, assessing which provided superior results. In the first, the bone section was placed in a custom-made 0.4 mm recess type B aluminum carrier (Wohlwend GmbH, Sennwald, Switzerland) and closed with the flat side of a standard gold-coated copper type B carrier (BALTIC Preparation, Wetter, Germany) (Fig. 2B, left). In the second configuration, the section was
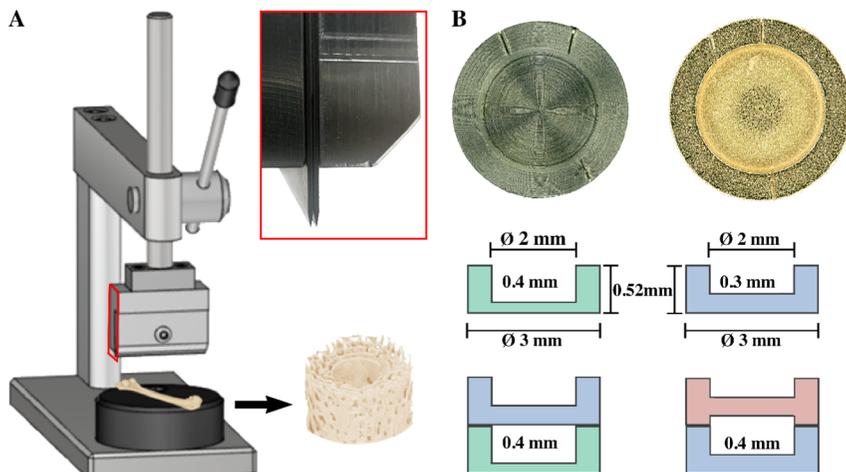
Fig. 2 Sample preparation for high-pressure freezing of quail femur cross-sections at EDD12. (A) Custom-designed double-blade guillotine used to cut 400 μm-thick bone cross-sections. (B) Left: Custom-made 0.4 mm recess type B aluminum carrier marked at three locations on the rim. The sandwich configuration is made by adding the flat side of a gold-coated copper type B carrier on top. Right: An alternative configuration where the section was placed in a gold-coated copper type B carrier, still marked at three locations on the rim, and covered with a type A carrier on the 100 μm recessed side. In both setups, the total cavity thickness is 400 μm.

positioned in a regular gold-coated copper type B carrier and covered with a type A carrier on the 100 μm recessed side (BALTIC Preparation, Wetter, Germany) (Fig. 2B, right). In both setups, the remaining volume within the carrier was filled with 20 wt% dextran (Sigma, 31390) as a cryoprotectant. The prepared samples were cryo-immobilized using a Leica ICE high-pressure freezing machine (Leica Microsystems, Vienna, Austria) within 5 minutes of the animal's sacrifice.

2.4. Cryogenic Light Microscopy (cryo-LM)

The frozen sample carriers were manually opened within the cryo-CLEM transfer shuttle (Leica Microsystems, Vienna, Austria) at liquid nitrogen temperature. This was achieved by carefully using tweezers to push the carriers apart. Once opened, the bottom carrier containing the sample was loaded into a custom-designed cartridge for transfer into the Leica DM6 FS Thunder cryo-microscope (Leica Microsystems, Vienna, Austria). The microscope is equipped with a HC PL APO 50×/0.90 DRY objective (0.9 numerical aperture) and a Leica DFC9000GT-VSC14964 camera. Image acquisition was conducted using custom settings with two fluorescence filters: GFP (emission wavelength 525 nm) and REF (emission wavelength 450 nm). Images were captured at a frame size of 1024 × 1024 pixels with a pixel size of 0.25 μm. Z-steps were adjusted for each sample to optimize resolution, resulting in step sizes of either 0.547 μm (100 steps) or 0.353 μm (70 steps). The exposure time ranged between 5 and 20 ms for channel 1 (GFP, green fluorescence) and 2 ms for channel 2 (REF, reflection, grey), using identical gain settings optimized for low noise and high well capacity. To enhance image quality and facilitate the subsequent correlation with the cryo-FIB-SEM, regions of

interest (ROIs) were processed using the Lightning Thunder processing tool (Instant Computational Clearing, ICC) available with the LAS X software (Leica Microsystems, Vienna, Austria). Additional processing included the use of Mosaic Merge for stitching images of marker scans on the carrier's rim and Projection tools for generating composite views of the ROIs. This composite image was saved as a TIFF. This approach ensured precise alignment and improved correlation across imaging modalities.

2.5. Cryogenic Focused Ion Beam-Scanning Electron Microscopy (cryo-FIB-SEM)

After light microscopy imaging, the cartridge was transferred into a modified FIB-SEM blank specimen cryo holder (Leica Microsystems, Vienna, Austria), which is designed to fit the cartridge, in the Leica EM VCM loading station (Leica Microsystems, Vienna, Austria). Using the VCT500 shuttle, the sample was then transferred to the ACE600 (Leica Microsystems, Vienna, Austria) for sputter coating with a 10 nm layer of carbon followed by a similar layer of platinum. Finally, the samples were transferred to the Zeiss Crossbeam 540 (Zeiss Microscopy GmbH, Oberkochen, Germany) using the VCT500 shuttle. Throughout the workflow, the bone samples were maintained at a temperature below −145 °C. Atlas 5 software (Fibics, Ottowa, Canada) was used to correlate the composite image from light microscopy and electron microscopy. First, an overview of the carrier containing the sample was acquired at 2 kV and 90 pA, with a working distance of 3 mm. The composite image was then imported, overlaid and manually rotated in order to align the three pre-marked rim positions between the two imaging modalities. The holder was subsequently tilted to 54° and elevated to a distance of 5.2 mm, corresponding to the coincident point of the electron and ion beams. Finally, the stage was automatically moved to the target position defined by the overlay of the fluorescence signal.

2.6. Serial Surface View (SSV) imaging

FIB-SEM serial surface view imaging was performed using SmartFIB software (Zeiss Microscopy GmbH, Oberkochen, Germany) on two femoral midshaft sections. In total, three stacks were acquired based on the correlation with the fluorescence signal. For each stack, a trench approximately 40 μm long and 80 μm wide was milled at 30 nA. The exposed surface was polished and imaged with a lower ion beam current (700 pA). The electron beam was then focused on the polished exposed tissue at 2 keV, 90 pA for all stacks. Sequential imaging was performed using the "slice and view" protocol, with the pixel size set to 8 nm in the x and y directions prior to data collection. The slice spacing (z direction) was also set at 8 nm to ensure an isometric voxel size. All stacks were acquired at an image resolution of 4096×3072 pixels in 8-bit greyscale. The dual-channel imaging mode was used, allowing simultaneous acquisition of signals from the mixed InLens/secondary electron (SE) detector and the backscattered electron (BSE) detector.

2.7. Image processing and segmentation

Image alignment, processing, and segmentation were carried out using Dragonfly software, Version 2024 (Object Research Systems (ORS) Inc., Montreal, Canada).

Automatic alignment of both BSE and mixed InLens/SE images was achieved through the slice registration panel using the sum of square differences (SSD) method, with manual adjustments applied as needed. A vertical destriping filter was employed to mitigate curtaining artifacts caused by the beam during the milling process. To enhance structural visualization, contrast enhancement and noise reduction were performed in 3D using a convolution filter. Additionally, the contrast in mixed InLens/SE image stacks was further refined through the application of the contrast-limited adaptive histogram equalization (CLAHE) filter. For segmentation, denser and brighter regions in the BSE stacks were segmented using the segmentation wizard module in Dragonfly. This process involved training on five to seven slices with varying input sizes per dataset, followed by manual corrections with the brush tool. In mixed SE/InLens stacks, features such as vesicles, nuclei, and cells were segmented using the active contour method available within the Dragonfly software.

2.8. Post-acquisition correlation of light and electron microscopy volumes

Post-acquisition correlation of light microscopy and electron microscopy image volumes presents inherent challenges due to the significant differences in resolution and field of view between these modalities (Fig. 3A). A further complication arises because the acquired LM and FIB-SEM volumes are not aligned within the same coordinate system. Specifically, the LM volume is acquired in a plane parallel to the sample surface, whereas the FIB-SEM volume is imaged in a plane perpendicular to the sample surface (Fig. 3A-iii).

To resolve these discrepancies and facilitate volume registration, we developed a standardized workflow using Dragonfly software, Version 2024 (Object Research Systems (ORS) Inc., Montreal, Canada). Briefly, the initial coordinate system of the LM fluorescence volume (XYZ_{LM}^{i}) is first transformed to the XYZ_{LM}^{t} system using the "Axis Transformation" command, aligning the LM volume's sample surface with that of the FIB-SEM volume (Fig. 3B, steps 1 and 2). The LM volume is then rotated around its Z_{LM}^{t} axis by an angle θ (Fig. 3B, step 3), determined based on the overlay of both modalities (from Atlas) (Fig. 3A-i). Finally, the LM volume is carefully translated until the ROI landmark is precisely aligned with the corresponding features in the FIB-SEM volume (Fig. 3B, step 4).

3. Results and discussion

Fig. 4 shows our cryo-CLEM workflow encompassing the entire process from sample preparation to image analysis. This workflow enabled us to reliably correlate fluorescence signals obtained from cryo-light microscopy with high-resolution images from cryo-FIB-SEM. With the custom-made holders designed specifically for both light and electron microscopy, we were able to significantly reduce the transfer time between imaging modalities, thereby improving efficiency and maintaining sample stability and integrity.

Although cryo-CLEM workflows using HPF carriers have been previously established,[18,19] their successful implementation often requires adaptations based on the specific equipment and tools available in each laboratory. Variations in cryo-light microscopes, FIB-SEM systems, sample transfer devices, and sample holders necessitate adjustments to ensure cohesive workflow execution. From
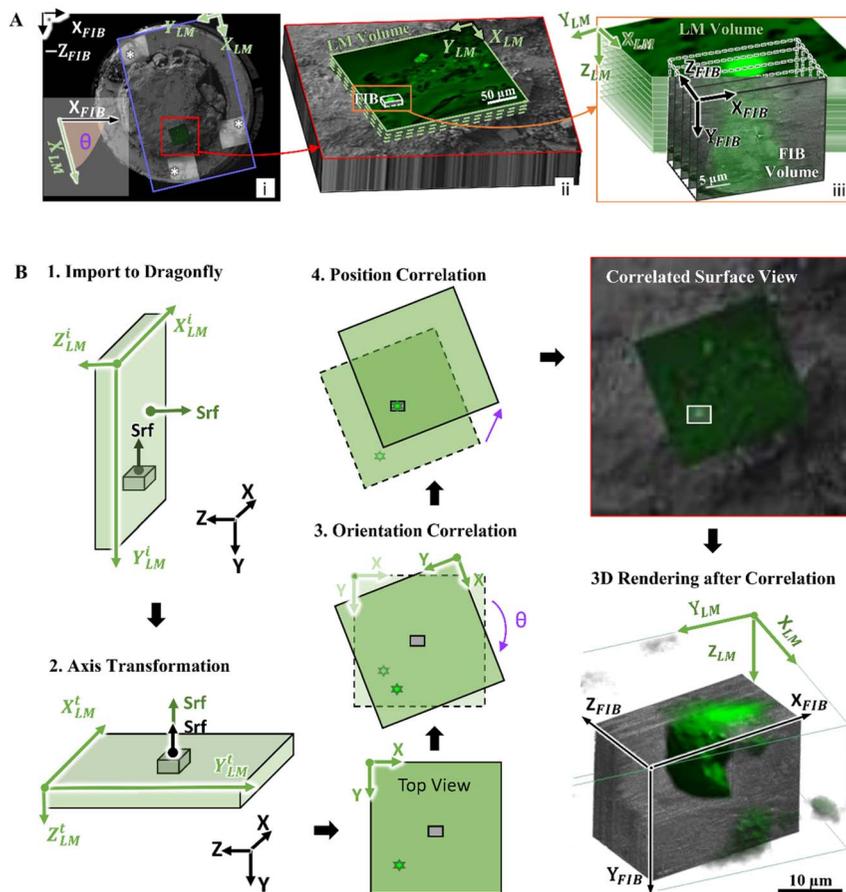
Fig. 3 Post-acquisition correlation for LM and FIB-SEM volumes. (A) Atlas overlay image (A-i) which superimposes images from the two modalities, demonstrating the relative positioning of the two dataset volumes (A-ii) and their respective native coordinate systems (A-iii). In both modalities, the XY plane is the image acquisition plane, while the Z direction corresponds to the axis along which serial images are captured. (B) Schematic representation of the post-acquisition correlation process using Dragonfly. The green boxes represent the LM fluorescence image, while the grey boxes represent the FIB-SEM volume. Upon importing to Dragonfly (1), the sample surfaces (Srf) of the two volumes are initially misaligned due to differences in their native coordinate systems. Therefore, to correlate the ROIs between the two volumes, the LM volume undergoes a series of transformations, including axis realignment (2), rotation based on the θ angle measured between the LM and FIB-SEM overlay in Atlas (A-i) (3), and finally translation (4). The translation is achieved by precisely correlating a landmark in the LM volume (green star) with corresponding features in the FIB-SEM volume.

a technical point of view, the gold-coated carriers were more stable once placed in our custom-designed cartridge, probably because the aluminum ones shrink slightly in liquid nitrogen. Nevertheless, the correlation between imaging modalities and the data acquired was similar in both cases. These fiducial markers provided spatial references that facilitated accurate correlation between light microscopy (fluorescence) and electron microscopy (FIB-SEM) datasets
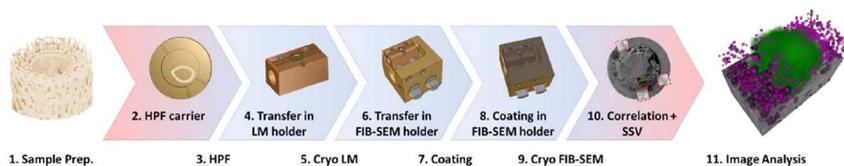
Fig. 4 Schematic representation of the key steps of our cryo-CLEM workflow from sample preparation to image analysis.

(Fig. 5A–C). In cryo-CLEM, several factors can limit the resolution and quality of the acquired images, despite the theoretical resolution of the microscope suggesting otherwise. While this technique offers improved resolution and fluorophore intensity compared to room temperature imaging,[28] it is constrained by the lack of high-numerical-aperture objectives compatible with cryogenic conditions. As a result, the actual resolution achievable in cryo-CLEM is often lower than its theoretical limits.[29,30] Despite these limitations, we show here that the fluorescence signal from QH1-labeled endothelial cells successfully localized regions corresponding to vascular structures when observed in electron
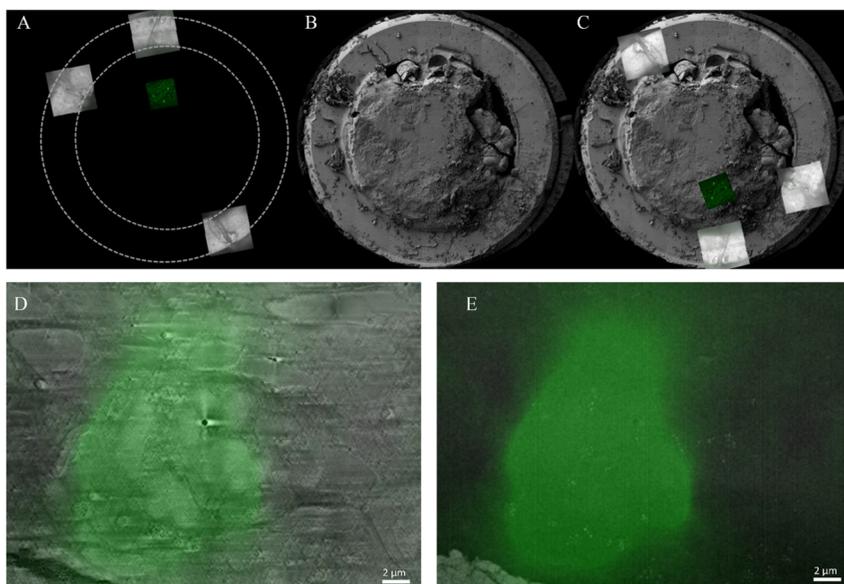

Fig. 5 Workflow for correlating fluorescence microscopy and electron microscopy datasets. (A) Overview image from light microscopy showing three pre-marked positions (white) on the high-pressure freezing (HPF) carrier rim, used as fiducial markers for spatial registration across imaging modalities. The green fluorescence signal highlights QH1-labeled endothelial cells. (B) FIB-SEM overview of the same sample before fluorescence alignment. (C) Correlated FIB-SEM image with overlaid fluorescence signal (green) localized to the ROI corresponding to vascular structures, rotated and aligned based on the rim markers. (D) High-resolution correlation of fluorescence microscopy (green) with the mixed-InLens/SE FIB-SEM image, confirming the localization of vascular structures. (E) Same image as (D) but using the BSE detector. Denser particles (which appear brighter) are visible in the area showing a high-fluorescence signal.

microscopy (Fig. 5D and E). This methodological precision enabled the acquisition of big volumetric electron microscopy data (thousands of μm^3) from targeted regions of interest (ROIs) with high confidence. The consistent alignment
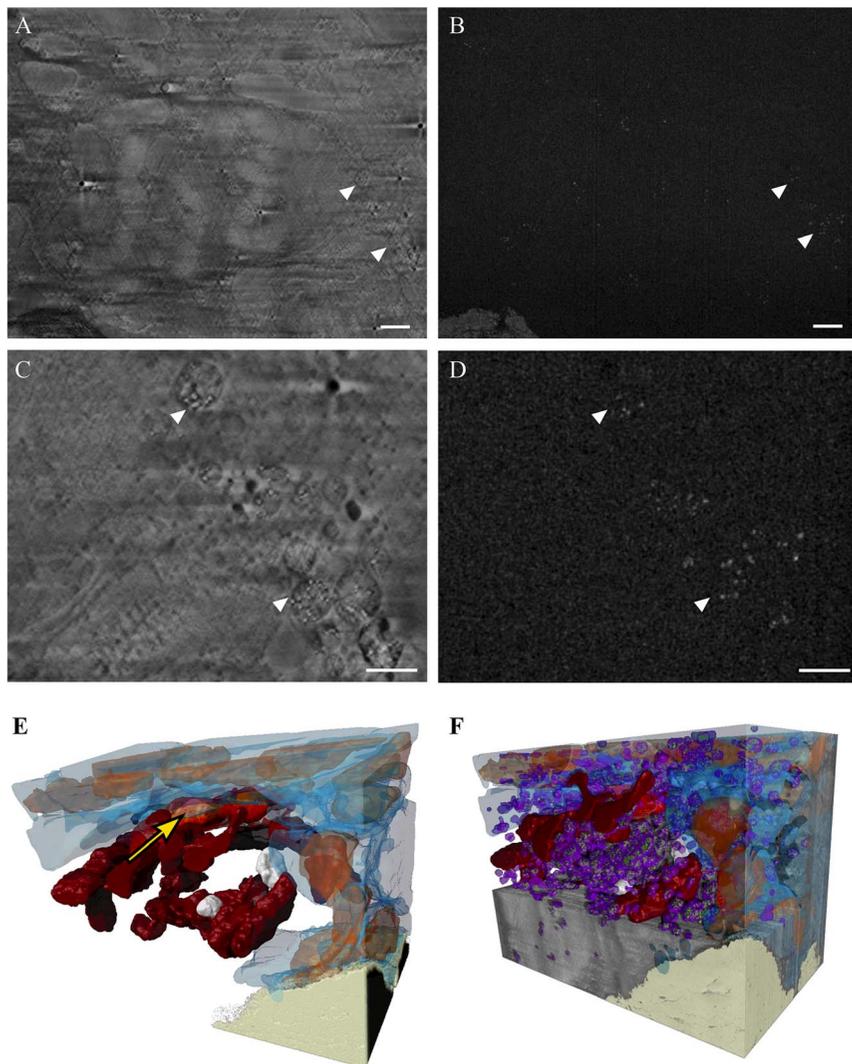

Fig. 6   FIB-SEM images of vesicles containing mineral precursors within the vasculature. (A) Image acquired with the InLens/SE detector showing the well-defined membrane of different components of the blood vessels. (B) Same image as (A) acquired with the backscattered electron (BSE) detector revealing electron-dense content, consistent with mineral precursors. (C and D) Enlargement of (A) and (B), respectively. (E and F) Perspective renderings of a 3D stack showing in (E) the structural organization consistent with known features of blood vessels, including endothelial cells (in blue) and erythrocytes (yellow arrow) with their nucleus (orange). Within the luminal spaces, larger (dark red) and smaller (white) structures are visible. (F) Numerous vesicles containing electron-dense material are observed both within the vascular lumen and in association with the endothelial cells lining the blood vessels (scale bar: 1 µm).

between imaging modalities ensured high confidence in identifying and analyzing vascularized tissues in electron microscopy volumes, validating the robustness of our workflow for studying vascular networks in the context of bone development.

Within the blood vessels defined by a more intense fluorescent area, we observed structures resembling granulocytes (Fig. 5D and E; Fig. 6A and B). These cells, which are characterized by their distinctive multi-lobed nuclei and cytoplasmic granules, are the most abundant leukocyte type in the peripheral blood of birds.[31,32] In addition to granulocytes, we also identified erythrocytes, which are distinguished by their oval shape and, unlike mammalian red blood cells, retain a nucleus throughout their lifespan[33,34] (Fig. 6E and F).

More intriguingly, surrounding these capillary structures, we observed numerous membrane-bound structures containing electron-dense material, consistent with mineral precursors (Fig. 6C and D). These vesicles, with a diameter ranging from 500 nm to 1 µm, were predominantly located within the vascular lumen, but were also found within the endothelial cells lining the blood vessels (Fig. 6F). Their presence aligns with studies reporting mineral-containing vesicles of similar sizes within blood vessels, serum, and bone-forming cells during bone development.[35–37] Hence, the presence of these vesicles aligns with the hypothesis that mineral precursors are transported *via* vesicular pathways within the vasculature, playing a key role in the process of bone mineralization. It has been shown that this vascular involvement extends to the growth plate, where mineral particles are observed in blood serum and vessel walls, with continuous pathways connecting blood vessels to mineralizing cartilage.[38] The localization of these vesicles within both the vascular lumen and endothelial cells suggests a complex and highly regulated system for the transport and delivery of mineral precursors. These observations support the hypothesis that the vasculature plays an active role in bone mineralization, not only as a pathway for the transport of mineral precursors, but also as a site for regulatory processes that direct the deposition of minerals in developing tissues.[6,39]

Interestingly, the vesicles within the blood vessels exhibited a distinct directional alignment (Fig. 7). This phenomenon is likely attributable to the laminar flow, which is characteristic of blood movement in smaller vessels, such as capillaries. In laminar flow, blood moves in parallel layers with minimal turbulence, and these layers exhibit different velocities due to friction. This velocity gradient between adjacent layers of blood fluid generates a stable and parabolic shear stress profile across the flow. Such a shear environment influences the behavior and orientation of cells and subcellular structures suspended in the blood plasma. The viscous nature of blood plays a critical role in this process, as it governs the interaction between layers of flowing fluid and the particles within them.[40–42] It is well documented that shear stress influences the transport and organization of cellular and subcellular structures in the blood. For example, studies have shown that red blood cells and platelets align and deform in response to shear stress, optimizing their transport through narrow capillaries.[42,43] Similarly, vesicles containing mineral precursors may respond to these mechanical environments by aligning within the laminar flow. This alignment not only indicates that these observed structures are indeed within the blood vessels, but also suggests an active role of flow dynamics in organizing vesicular transport mechanisms. The close interplay between blood flow, viscosity, and vesicle alignment underscores the
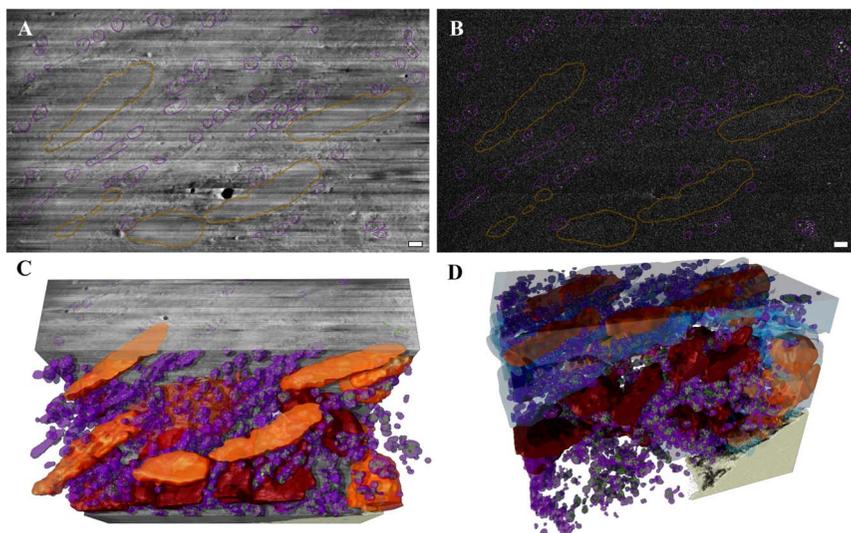
Fig. 7   Vesicles' alignment inside the blood vessels. (A) Image acquired with the InLens/SE detector showing some elongated components (outlined in orange) of the cells and vasculature with numerous vesicles aligned (outlined in purple). (B) Same image as (A) acquired with the backscattered electron (BSE) detector, revealing the electron-dense mineral precursors found within the vesicles. (C and D) 3D perspective rendering showing the vesicles' distribution, as well as the elongated and aligned blood structures (scale bar: 1 μm).

mechanobiological complexity of mineralization processes and highlights the vasculature's active role in skeletal development.[6]

The presence of vesicles containing mineral precursors within the vasculature strongly supports the hypothesis that blood vessels play a direct role in transporting these precursors to bone formation sites. This transport pathway within vesicles may complement the diffusion of free ions, providing a more controlled and efficient mechanism for mineral delivery to developing bone.[35]

During avian embryological development, the highly vascularized chorioallantoic membrane (CAM) plays a crucial role in calcium transport from the eggshell to the developing embryo. In chicken embryos, it has been shown that the CAM fully surrounds the embryo by EDD11 and becomes actively involved in calcium transport around EDD13, coinciding with a marked increase in skeletal growth.[25,44] While a similar developmental timeline has not been explicitly defined for quail, Ainsworth et al. (2010)[45] provided a comparative analysis of developmental stages between quail and chicken embryos, demonstrating that the growth rate in quail embryos begins to increase significantly at EDD12. Based on this, the onset of active calcium uptake from the eggshell in quail can be inferred to occur around this stage. This timing could explain the abundance of mineral-containing vesicles observed in the vasculature at EDD12 in our study. As calcium demand increases to support rapid skeletal growth, vesicle-mediated transport may represent a crucial mechanism for efficiently delivering mineral precursors in quail. Future studies should examine different embryonic days to study changes in the dynamics of calcium transport over developmental time and thereby further elucidate the role of vesicular transport in this process.

However, some limitations need to be addressed: for instance, the double-blade guillotine used in sample preparation requires further optimization to produce thinner sections, which would facilitate ultrastructural analysis by transmission electron microscopy (TEM). Nonetheless, our results are highly encouraging from both methodological and scientific perspectives. The workflow we developed provides a valuable framework for future studies, not only in the context of embryonic bone development but also in other systems where vascularization plays a critical role in tissue development, mineralization, and disease.

4.   Conclusions

Using the cryo-CLEM workflow, we discover numerous vesicles within the vasculature of the quail embryo at EDD12, containing mineral precursors at a stage where the chorioallantoic membrane (CAM) begins to remove most of the calcium from the eggshell. This suggests that the vasculature plays a crucial role in the calcium transport in supporting rapid skeletal growth, a characteristic of fast-developing quail embryos. The alignment of these vesicles along the direction of blood flow highlights the influence of vascular dynamics on mineral transport. These insights result from the ability to visualize these mineral-containing structures in their near-native state, elucidating the contribution of vascular pathways to mineralization.

Data availability

Data are available upon request to the corresponding author.

Conflicts of interest

There are no conflicts to declare.

Acknowledgements

References

1 A. Grosso, M. G. Burger, A. Lunger, D. J. Schaefer, A. Banfi and N. Di Maggio, It Takes Two to Tango: Coupling of Angiogenesis and Osteogenesis for Bone Regeneration, *Front. Bioeng. Biotechnol.*, 2017, **5**, 68.

2 A. P. Kusumbe, S. K. Ramasamy and R. H. Adams, Coupling of angiogenesis and osteogenesis by a specific vessel subtype in bone, *Nature*, 2014, **507**(7492), 323–328.

3 J. Filipowska, K. A. Tomaszewski, Ł. Niedźwiedzki, J. A. Walocha and T. Niedźwiedzki, The role of vasculature in bone development, regeneration and proper systemic functioning, *Angiogenesis*, 2017, **20**, 291–302.

4 J. G. J. Hoenderop, B. Nilius and R. J. M. Bindels, Calcium Absorption Across Epithelia, *Physiol. Rev.*, 2005, **85**(1), 373–422.

5 C. J. Percival and J. T. Richtsmeier, Angiogenesis and intramembranous osteogenesis, *Dev. Dyn.*, 2013, **242**, 909–922.

6 B. Thompson and D. A. Towler, Arterial calcification and bone physiology: role of the bone–vascular axis, *Nat. Rev. Endocrinol.*, 2012, **8**(9), 529–543.

7 C. Owen-Woods and A. Kusumbe, Fundamentals of bone vasculature: Specialization, interactions and functions, *Semin. Cell Dev. Biol.*, 2022, **123**, 36–47.

8 E. A. Streeten and M. L. Brandi, Biology of bone endothelial cells, *Bone Miner.*, 1990, **10**(2), 85–94.

9 C. Carulli, M. Innocenti and M. L. Brandi, Bone Vascularization in Normal and Disease Conditions, *Front. Endocrinol.*, 2013, **4**, 106.

10 S. Jun, H.-J. Ro, A. Bharda, S. I. Kim, D. Jeoung and H. S. Jung, Advances in Cryo-Correlative Light and Electron Microscopy: Applications for Studying Molecular and Cellular Events, *Protein J.*, 2019, **38**(6), 609–615.

11 A. Bieber, C. Capitanio, F. Wilfling, J. Plitzko and P. S. Erdmann, Sample Preparation by 3D-Correlative Focused Ion Beam Milling for High-Resolution Cryo-Electron Tomography, *J. Visualized Exp.*, 2021, **176**, e62886.

12 J. A. Pierson, J. E. Yang and E. R. Wright, Recent advances in correlative cryo-light and electron microscopy, *Curr. Opin. Struct. Biol.*, 2024, **89**, 102934.

13 G. Wolff, C. Hagen, K. Grünewald and R. Kaufmann, Towards correlative super-resolution fluorescence and electron cryo-microscopy, *Biol. Cell*, 2016, **108**(9), 245–258.

14 J. Mahamid, R. Schampers, H. Persoon, A. A. Hyman, W. Baumeister and J. M. Plitzko, A focused ion beam milling and lift-out approach for site-specific preparation of frozen-hydrated lamellas from multicellular organisms, *J. Struct. Biol.*, 2015, **192**(2), 262–269.

15 A. J. Noble and A. de Marco, Cryo-focused ion beam for *in situ* structural biology: State of the art, challenges, and perspectives, *Curr. Opin. Struct. Biol.*, 2024, **87**, 102864.

16 D. Studer, B. M. Humbel and M. Chiquet, Electron microscopy of high pressure frozen samples: bridging the gap between cellular ultrastructure and atomic resolution, *Histochem. Cell Biol.*, 2008, **130**(5), 877–889.

17 R. Dahl and L. A. Staehelin, High-pressure freezing for the preservation of biological structure: Theory and practice, *J. Electron Microsc. Tech.*, 1989, **13**(3), 165–174.

18 N. Scher, K. Rechav, P. Paul-Gilloteaux and O. Avinoam, In situ fiducial markers for 3D correlative cryo-fluorescence and FIB-SEM imaging, *iScience*, 2021, **24**(7), 102714.

19 M. de Beer, D. Daviran, R. Roverts, L. Rutten, E. Macías-Sánchez, J. R. Metz, *et al.*, Precise targeting for 3D cryo-correlative light and electron microscopy volume imaging of tissues using a FinderTOP, *Commun. Biol.*, 2023, **6**(1), 510.

20 X. Heiligenstein, M. de Beer, J. Heiligenstein, F. Eyraud, L. Manet, F. Schmitt, *et al.*, Chapter 6 - HPM live μ for a full CLEM workflow, *Methods in Cell Biology*, ed. Müller-Reichert T. and Verkade P., Academic Press, vol. 162, 2021, pp. 115–49.

21 P. Nowak-Sliwinska, T. Segura and M. L. Iruela-Arispe, The chicken chorioallantoic membrane model in biology, medicine and bioengineering, *Angiogenesis*, 2014, **17**(4), 779–804.

22 R. S. Tuan, M. J. Carson, J. Józefiak, K. A. Knowles and B. A. Shotwell, Calcium-transport function of the chick embryonic chorioallantoic membrane. I. *In vivo* and *in vitro* characterization, *J. Cell Sci.*, 1986, **82**, 73–84.

23 D. Ribatti, A. Frigeri, B. Nico, G. P. Nicchia, M. De Giorgis, L. Roncali and M. Svelto, Aquaporin-1 expression in the chick embryo chorioallantoic membrane, *Anat. Rec.*, 2002, **268**(2), 85–89.

24 J. R. Coleman, S. M. DeWitt, P. Batt and A. R. Terepka, Electron probe analysis of calcium distribution during active transport in chick chorioallantoic membrane, *Exp. Cell Res.*, 1970, **63**(1), 216–220.

25 R. S. Tuan, Mechanism and regulation of calcium transport by the chick embryonic chorioallantoic membrane, *J. Exp. Zool.*, 1987, **1**, 1–13.

26 R. S. Tuan, Carbonic Anhydrase and Calcium Transport Function of the Chick Embryonic Chorioallantoic Membrane, *Ann. N. Y. Acad. Sci.*, 1984, **429**(1), 459–472.

27 L. Pardanaud, C. Altmann, P. Kitos, F. Dieterlen-Lievre and C. A. Buck, Vasculogenesis in the early quail blastodisc as studied with a monoclonal antibody recognizing endothelial cells, *Development*, 1987, **100**(2), 339–349.

28 R. Kaufmann, C. Hagen and K. Grünewald, Fluorescence cryo-microscopy: current challenges and prospects, *Curr. Opin. Chem. Biol.*, 2014, **20**, 86–91.

29 L. Wang, B. Bateman, L. C. Zanetti-Domingues, A. N. Moores, S. Astbury, C. Spindloe, *et al.*, Solid immersion microscopy images cells under cryogenic conditions with 12 nm resolution, *Commun. Biol.*, 2019, **2**(1), 74.

30 R. Faoro, M. Bassu, Y. X. Mejia, T. Stephan, N. Dudani, C. Boeker, *et al.*, Aberration-corrected cryoimmersion light microscopy, *Proc. Natl. Acad. Sci. U. S. A.*, 2018, **115**(6), 1204–1209.

31 A. Witkowski and J. P. Thaxton, Morphology of the Eosinophil in Japanese Quail1,2, *Poult. Sci.*, 1981, **60**(7), 1587–1590.

32 E. Kolesnik, M. Derkho, V. Strizhikov, S. Strizhikova, T. Sereda, F. Gizatullina and M. Rebezov, Functional morphology of birds' blood leukocytes, *J. Exp. Biol. Agric. Sci.*, 2020, **8**, S374–S380.

33 C. G. Scanes, Chapter 10 – Blood,in *Sturkie's Avian Physiology*, ed. Scanes C. G., Academic Press, San Diego, 6th edn, 2015, pp. 167–91.

34 M. Tadjalli, S. Nazifi and A. Eemanparvar, Normal cellular morphology of the blood of Japanese quail (Coturnix coturnix japonica), *Comp. Clin. Pathol.*, 2003, **12**(2), 102–105.

35 M. Kerschnitzki, A. Akiva, A. B. Shoham, N. Koifman, E. Shimoni, K. Rechav, *et al.*, Transport of membrane-bound mineral particles in blood vessels during chicken embryonic bone development, *Bone*, 2016, **83**, 65–72.

36 E. Raguin, R. Weinkamer, C. Schmitt, L. Curcuraci and P. Fratzl, Logistics of Bone Mineralization in the Chick Embryo Studied by 3D Cryo FIB-SEM Imaging, *Advanced Science*, 2023, **10**(22), 2301231.

37 J. Mahamid, A. Sharir, D. Gur, E. Zelzer, L. Addadi and S. Weiner, Bone mineralization proceeds through intracellular calcium phosphate loaded vesicles: A cryo-electron microscopy study, *J. Struct. Biol.*, 2011, **174**(3), 527–535.

38 H. Haimov, E. Shimoni, V. Brumfeld, M. Shemesh, N. Varsano, L. Addadi and S. Weiner, Mineralization pathways in the active murine epiphyseal growth plate, *Bone*, 2020, **130**, 115086.

39 I. Azoidis, S. C. Cox and O. G. Davies, The role of extracellular vesicles in biomineralisation: current perspective and application in regenerative medicine, *J. Tissue Eng.*, 2018, **9**, 2041731418810130.

40 O. K. Baskurt and H. J. Meiselman, Blood Rheology and Hemodynamics, *Semin. Thromb. Hemostasis*, 2003, **29**(05), 435–450.

41 H. Sakai, A. Sato, N. Okuda, S. Takeoka, N. Maeda and E. Tsuchida, Peculiar flow patterns of RBCs suspended in viscous fluids and perfused through a narrow tube (25 μm), *Am. J. Physiol. Heart Circ. Physiol.*, 2009, **297**(2), H583–H589.

42 T. W. Secomb, Blood Flow in the Microcirculation, *Annu. Rev. Fluid Mech.*, 2017, **49**, 443–461.

43 J. Mauer, S. Mendez, L. Lanotte, F. Nicoud, M. Abkarian, G. Gompper and D. A. Fedosov, Flow-Induced Transitions of Red Blood Cell Shapes under Shear, *Phys. Rev. Lett.*, 2018, **121**(11), 118103.

44 Q. Huang, R. Yang, Q. Wang, H. Teng, H. Song, F. Geng and P. Luo, Transcriptome-based insights into the calcium transport mechanism of chick chorioallantoic membrane, *Food Sci. Hum. Wellness*, 2022, **11**(2), 383–392.

45 S. J. Ainsworth, R. L. Stanley and D. J. R. Evans, Developmental stages of the Japanese quail, *J. Anat.*, 2010, **216**, 3–15.